

On the computation of the demagnetization tensor for uniformly magnetized particles of arbitrary shape. Part II: numerical approach

S. Tandon^a, M. Beleggia^b, Y. Zhu^b, M. De Graef^{a,*}

^a Department of Materials Science and Engineering, Carnegie Mellon University, 5000 Forbes Avenue, Pittsburgh, PA, 15213-3890, USA

^b Materials Science Department, Brookhaven National Laboratory, Upton, NY 11973, USA

Received 17 July 2003; received in revised form 24 August 2003

Abstract

In Part I, we described an analytical approach to the computation of the demagnetization tensor field for a uniformly magnetized particle with an arbitrary shape. In this paper, Part II, we introduce two methods for the numerical computation of the demagnetization tensor field. One method uses a Fourier space representation of the particle shape, the other starts from the real space representation. The accuracy of the methods is compared to theoretical results for the demagnetization tensor of the uniformly magnetized cylinder with arbitrary aspect ratio. Example computations are presented for the hexagonal plate, the truncated paraboloid, and a so-called “Pac-Man” shape, recently designed for MRAM applications. Finally, the magnetostatic self-energy of a uniformly magnetized regular polygonal disk of arbitrary order is analyzed. A linear relation is found between the order of the polygon and the critical aspect ratio for in-plane vs. axial magnetization states.

© 2003 Elsevier B.V. All rights reserved.

PACS: 41.20.Gz; 75.30.Gw; 75.40.Mg

Keywords: Demagnetization tensor field; Shape amplitude; Polygonal disk; Numerical algorithm; Demagnetization energy

1. Introduction

The computation of the magnetic induction inside and surrounding a uniformly magnetized particle of arbitrary shape requires knowledge of the demagnetization tensor field, also known as the point-function demagnetization tensor [1]. In

Part I of this two-paper series [2], we have shown analytical computations of the demagnetization tensor field (DTF) of the cylinder. This is a special shape for which the equations can be solved analytically. In most cases, however, numerical methods must be used to determine the tensor field. In this paper, Part II, we will introduce two different numerical procedures for the computation of the DTF. In Section 2, we summarize the theoretical model for the DTF and related quantities, the magnetostatic energy and the

*Corresponding author. Tel.: +1-412-268-8527; fax: +1-412-268-7596.

E-mail address: degrae@cmu.edu (M. De Graef).

magnetometric demagnetization tensor. Section 3.1 deals with a solution method which can be used if an analytical expression for the shape amplitude is available. We also introduce an improved version of the latter case, in which a filter function is applied in Fourier space to suppress Gibbs-like oscillations in the real space DTF. In Section 3.2, we introduce a numerical procedure which starts from the shape function of the object, and employs numerical fast Fourier transforms (FFT) to determine the DTF. Throughout this paper, we compare the numerical results with analytical computations based on the expression for the DTF of the uniformly magnetized cylinder of Part I [2]. We conclude the paper with a computation of the critical aspect ratio for in-plane vs. out-of-plane magnetization for regular polygonal disks of arbitrary order.

2. Summary of the theoretical model

As shown by Beleggia and De Graef [3], the demagnetization tensor field for a uniformly magnetized particle with shape function $D(\mathbf{r})$ (also known as characteristic function) can be represented in Fourier space as follows:

$$N_{ij}(\mathbf{k}) = D(\mathbf{k}) \frac{k_i k_j}{k^2}, \quad (1)$$

where \mathbf{k} is the frequency vector, and $D(\mathbf{k})$ the shape amplitude (i.e., the Fourier transform of the shape function). In real space, the demagnetization tensor field is given by the inverse Fourier transform of Eq. (1):

$$N_{ij}(\mathbf{r}) \equiv \frac{1}{8\pi^3} \int d^3\mathbf{k} \frac{D(\mathbf{k})}{k^2} k_i k_j e^{i\mathbf{k}\cdot\mathbf{r}}. \quad (2)$$

The following relations were explicitly derived in Ref. [3]:

1. the trace of $N_{ij}(\mathbf{r})$ is equal to the shape function $D(\mathbf{r})$,
2. the demagnetization energy can be written in terms of the shape amplitude as

$$E_m = \frac{\mu_0 M_0^2}{16\pi^3} \int d^3\mathbf{k} \frac{|D(\mathbf{k})|^2}{k^2} (\hat{\mathbf{m}} \cdot \mathbf{k})^2, \quad (3)$$

with M_0 the magnitude of the magnetization and $\hat{\mathbf{m}}$ a unit magnetization vector;

3. the volume averaged (or magnetometric) demagnetization tensor is given by

$$\begin{aligned} \langle N \rangle_{ij} &= \frac{1}{V} \int_V d^3\mathbf{r} N_{ij}(\mathbf{r}) \\ &= \frac{1}{8\pi^3 V} \int d^3\mathbf{k} \frac{|D(\mathbf{k})|^2}{k^2} k_i k_j, \end{aligned} \quad (4)$$

where V is the volume of the particle.

3. Numerical methods for the computation of the demagnetization tensor field

3.1. Starting from the shape amplitude $D(\mathbf{k})$

The shape amplitude $D(\mathbf{k})$ can be computed analytically for many different particle shapes, among others: sphere [4], cylinder [4], truncated paraboloid [2], Platonic solids [5,6], and so on. When the shape amplitude is used to compute the DTF, one must select a 3D computational grid on which the tensor field will be calculated. In most cases, the use of FFT dictates that the dimensions of the grid be powers of 2, although such a requirement is no longer necessary when modern FFT algorithms are used (e.g., the FFTW package [7]). Since the shape function is a discontinuous function, its Fourier representation always requires an infinite support. Truncation of this support to a finite computational grid results in the familiar Gibbs oscillations near all discontinuities of the shape function. These oscillations are also present in the DTF, since the phases of the Fourier components $N_{ij}(\mathbf{k})$ are identical to those of the Fourier components $D(\mathbf{k})$. It is possible, however, to propose a Fourier space filter function, $g(\mathbf{k})$, which can be used to suppress the real space Gibbs oscillations.

The filter function is essentially a piecewise continuous cubic polynomial, used primarily for image reconstruction by parametric cubic convolution [8]. The function $g(k)$ is given by

$$g(k) = g_0(k) + \alpha g_1(k)$$

$$= \frac{3}{k^2} [\text{sinc}^2(k) - \text{sinc}(2k)] \\ + \alpha \frac{2}{k^2} [3\text{sinc}^2(2k) - 2\text{sinc}(2k) - \text{sinc}(4k)]. \quad (5)$$

where α is a parameter which can be chosen to optimize the reconstruction. The optimum value for image reconstruction is $\alpha = -0.5$ [8]. This filter function $g(k)$ is the one-dimensional (1D) Fourier transform of the piecewise continuous cubic polynomial

$$g(r) = g_0(r) + \alpha g_1(r), \quad (6)$$

with

$$g_0(r) = \begin{cases} (2|r| + 1)(|r| - 1)^2 & |r| < 1 \\ 0 & \text{elsewhere} \end{cases} \quad (7)$$

and

$$g_1(r) = \begin{cases} |r|^2(|r| - 1) & |r| < 1, \\ (|r| - 1)(|r| - 2)^2 & 1 < |r| < 2, \\ 0 & \text{elsewhere.} \end{cases} \quad (8)$$

Multiplication of the frequency spectrum of a 1D function with discontinuities with the filter function dramatically reduces the Gibbs phenomenon. As an example, consider the periodic step function which alternates between $+1$ and -1 . Its Fourier representation is given by

$$f(x) = \sum_{n=0}^{\infty} A_n \sin(n\pi x) \\ \text{with } \begin{cases} A_{2n} = 0 \\ A_{2n+1} = \frac{4}{\pi(2n+1)}. \end{cases} \quad (9)$$

When this series is truncated after 25 terms ($n = 25$), then the resulting function is shown in Fig. 1(a). An overshoot of 9% of the amount of the discontinuity occurs, and the function oscillates (Gibbs oscillations) around the values ± 1 elsewhere. If the Fourier coefficients are multiplied by the filter function, i.e., $A_n \rightarrow A_n g(k_n)$, then the resulting reconstructed function is significantly smoother, as shown for the values $\alpha = -0.5, 0.0$, and 0.5 in Fig. 1(b)–(d). The inset shows the details at the discontinuity, magnified by a factor of 4. When the number of terms is increased to $n = 50$,

the overshoot remains, and the filtered functions are shown on the second row of Fig. 1. It is evident that the filtered functions more closely approximate the step function, and that the reconstruction with $\alpha = 0$ creates the best approximation. For $\alpha = -0.5$ a small overshoot remains, whereas $\alpha = 0.5$ produces significant rounding at the discontinuity. For the remainder of this paper we will use the filter function in Eq. (5) with $\alpha = 0$. The same filter function can be used in three dimensions, provided the length of the frequency vector \mathbf{k} is used for k .

If we denote the tensor function $k_i k_j / k^2$ by $\kappa_{ij}(\mathbf{k})$, then, according to Eq. (1), the DTF is given by

$$N_{ij}(\mathbf{r}) = \mathcal{F}^{-1} [D(\mathbf{k}) \kappa_{ij}(\mathbf{k})]. \quad (10)$$

If an analytical version of $D(\mathbf{k})$ is available, then this equation should be replaced by a filtered version for all numerical work:

$$N_{ij}(\mathbf{r}) = \mathcal{F}^{-1} [D(\mathbf{k}) \kappa_{ij}(\mathbf{k}) g(|\mathbf{k}|)]. \quad (11)$$

To show the validity of the filtering approach, we compare analytical results for the uniformly magnetized cylinder with computational results with and without the filter function. The shape amplitude for a cylinder with radius R and aspect ratio $\tau = d/R$, with d the half-height, is given by (Part I and [4]):

$$D(\mathbf{k}) = 2V \frac{J_1(k_{\perp} R)}{k_{\perp} R} \text{sinc}(dk_z), \quad (12)$$

where $J_1(x)$ is the Bessel function of first order, k_{\perp} and k_z are the in-plane and orthogonal components of \mathbf{k} , resp., and $\text{sinc}(x) \equiv \sin(x)/x$. Fig. 2 shows the tensor element $N_{rr}(r, 0)$ for a cylinder with radius $R = 16$ (in pixels) and $\tau = 0.75$. The continuous curve represents the analytical solution, derived in Part I. The triangles on the left side of the figure correspond to the tensor element computed using Eq. (10) on a grid of 128^3 points. The truncation of the Fourier representation (12) after only 64 different frequencies results in strong Gibbs oscillations in the tensor element. Application of the Fourier filter in Eq. (11) reduces these oscillations and the resulting tensor element is shown on the right side of Fig. 2. There are only two points, one on either side of the discontinuity,

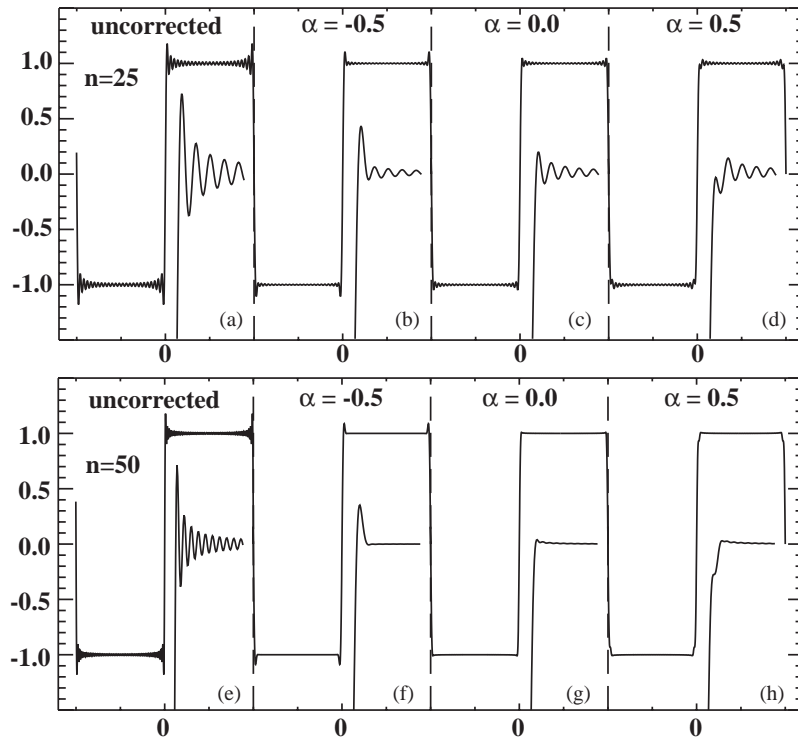


Fig. 1. (a) and (e) show the reconstruction of series expansion 9 for $n = 25$ and 50 , resp. The other curves are reconstructions using the filtered Fourier coefficients for three different values of the parameter α : -0.5 , 0.0 , and 0.5 . The insets show a magnified view of the discontinuity ($\times 4$).

for which the numerical value does not agree with the analytical result. If the number of grid points were doubled in each direction, then there would still be two incorrect points on either side of the discontinuity, but now those points would be closer to the discontinuity. In the limit of a continuous grid, the numerical result would coincide with the analytical solution. In practice, the number of grid points is determined by the available computing memory. The mean deviation between the analytical and numerical values for the tensor elements, excluding the points closest to the discontinuity, is typically about 0.1% for computations that include the filter function, and closer to 1% if the filter function is not used. These numbers are somewhat sensitive to the size of the cylinder relative to the size of the computational array. Smaller cylinders result in better agreement between theoretical values and numerical computations.

3.2. Starting from the shape function $D(\mathbf{r})$

Consider a 3D regular grid with N grid points along each axis. Any object for which the inside and outside can be unambiguously defined can be represented by an array of 1's and 0's, corresponding to the interior and exterior points, respectively. This is essentially a discrete representation of the shape function $D(\mathbf{r})$. Special topological cases, such as the Klein bottle and other non-orientable surfaces for which there is no inside or outside, cannot be dealt with in this formalism. The object need not be simply connected, so that hollow or shell-like objects can also be treated. One can also place multiple non-connected objects on the discrete array and compute the demagnetization tensor field for the set of all objects. Note that this then assumes that the magnetization direction used to contract the tensor to obtain the magnetic field, \mathbf{H} , must be identical in all objects that make

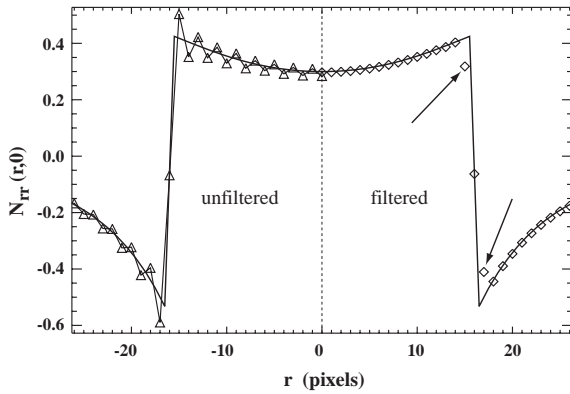


Fig. 2. Comparison between the analytical value of $N_{rr}(r, 0)$ for a cylinder with radius $R = 16$ and $\tau = 0.75$ (solid line), and a numerical simulation based on the discretized analytical expression of the shape amplitude in Eq. (12) (left curve). The Gibbs oscillations are clearly visible. After Fourier space filtering of the shape amplitude $D(\mathbf{k})$ with the function $g(k)$ of Eq. (5), the resulting numerical values are indicated by small diamonds on the right half of the figure. Only the two points arrowed deviate from the analytical solution; the others are within 1% of the analytical value.

up the complete array. If this is not the case, then the demagnetization tensor field must be computed for each object separately, then contracted with respect to the magnetization direction for that object, and the resulting magnetic field configurations for each object added together to obtain the magnetic field for the assembly of objects.

If we assume periodic boundary conditions, then the numerical Fourier transform of the 3D grid will approximate the analytical Fourier transform for the smaller spatial frequencies, but for higher spatial frequencies discrepancies will arise because of the finite support of the Fourier space. Only frequencies below the Nyquist frequency are meaningful. An inverse Fourier transform will recreate the original object *without Gibbs oscillations*, even when this object has discontinuities.

This observation leads to a simple numerical algorithm for the computation of the DTF on a discrete 3D grid:

1. create the discrete shape function $D(\mathbf{r})$ on the computational grid;
2. convert to Fourier space $D(\mathbf{k})$;

3. multiply by the $\kappa_{ij}(\mathbf{k})$ tensor field;
4. transform back to real space to obtain the DTF $N_{ij}(\mathbf{r})$.

As with all periodic continuation problems, care must be taken to properly select the size of the object with respect to the size of the computational grid. Near the edges of the grid, the values of the tensor field may be affected by the periodic boundary conditions.

As an example, consider the analytical solution for the uniformly magnetized cylinder in Part I. For a cylinder with radius $R = 16$ (pixels) and aspect ratio $\tau = 0.75$, the tensor field component $N_{rr}(r, 0)$ is shown as a continuous line in Fig. 3. When the tensor element is computed using the above algorithm, the function values on the left side of the figure are obtained (triangles). The agreement with the analytical solution is rather good, except at two points close to the discontinuity. The numerical result can be improved by considering a modified shape function $D(\mathbf{r})$. The modification consists of a smoothing operation, which is carried out for all grid points that are within a certain distance from the object surface. There are many possible smoothing options. A simple smoothing operation is carried out as follows: for each grid point located less than η

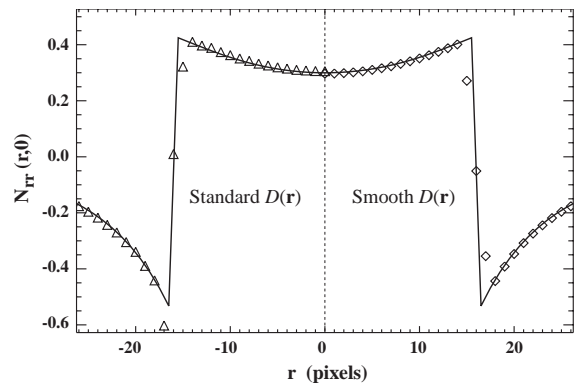


Fig. 3. Comparison between the analytical value of $N_{rr}(r, 0)$ for a cylinder with radius $R = 16$ and $\tau = 0.75$ (solid line), and a numerical simulation based on the shape function $D(\mathbf{r})$. On the left side, the shape function was discretized with only two intensity levels: 0 and 1. On the right, a smoother version of the shape function was used. The smoothed result should be compared with the Fourier space filtered result of Fig. 2.

grid spacings from the object surface (either inside or outside the object), the normal distance δ to the object surface is computed. For points on the inside of the object, the distance δ is taken to be negative. The shape function value at this grid point is then given by

$$D = \cos^2 \left(\pi \frac{(\delta + \eta)}{4\eta} \right). \quad (13)$$

This function smoothly goes from 1 inside the object to 0 outside the object. The tensor element $N_{rr}(r, 0)$ for the smoothed shape function is shown on the right in Fig. 3 (diamonds). The function values are identical to those for the unsmoothed shape function on the left, except for the two points near the discontinuity. For these points, the values are nearly identical to those obtained using the Fourier filtered shape amplitude (see right side of Fig. 2). The mean deviation between theoretical and numerical values, excluding the points closest to the discontinuity, is again about 0.1% when used with the smoothing operation, and closer to 1% without smoothing.

4. Example applications

In this section, we will apply the numerical formalisms described in Section 3 to a number of important shapes: the regular hexagonal plate, the truncated paraboloid, and a “pacman” thin plate. These shapes are shown schematically in Fig. 4(a)–(c). The regular hexagonal plate (Section 4.1) is an important building block for micromagnetic simulations, where it represents the shape of a finite element cell. The truncated paraboloid

(Section 4.2) approximates the shape of the tip of a magnetic force microscope. The “pacman” shape (Section 4.3) was recently proposed [9] as a novel shape for a sub-micron NiFe element for magnetic random access memory (MRAM) applications. We conclude this section with the numerical computation of the critical aspect ratio for polygonal disks.

4.1. The regular hexagonal plate

The shape amplitude of a regular hexagonal plate has been given in Eq. (14) of Part I, and is rather complicated. Since there is no straightforward analytical method to compute the real space DTF, starting from this shape amplitude, we apply the Fourier space filter function of Eq. (11). Two-dimensional section of the resulting DTF are shown in Fig. 5 for a plate with aspect ratio $\eta = \frac{2}{5}$ (computation carried out on a 128^3 grid). The top two rows show a grayscale representation of the tensor field elements for a plane going through the center of the hexagonal plate. All images have a common grayscale from -0.4 (black) to $+0.79$ (white). The axes in the lower corner of each image indicate the orientation of the two-dimensional section. The bottom two rows show two different sections (xy and xz) of the eigenvalues of the tensor field, ranked from smallest (λ_1) to largest (λ_3). The eigenvalues reveal the true symmetry of the tensor field.

4.2. The truncated paraboloid

The shape amplitude of the truncated paraboloid can be computed analytically, and the explicit

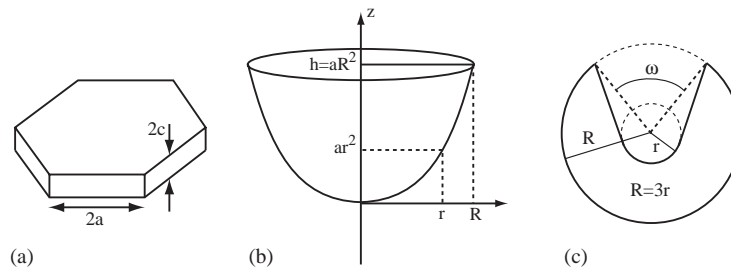


Fig. 4. Schematic illustration of the shapes for which example DTF computations are shown in Sections 4.1–4.3: (a) hexagonal plate, (b) truncated paraboloid and (c) “pacman” particle.

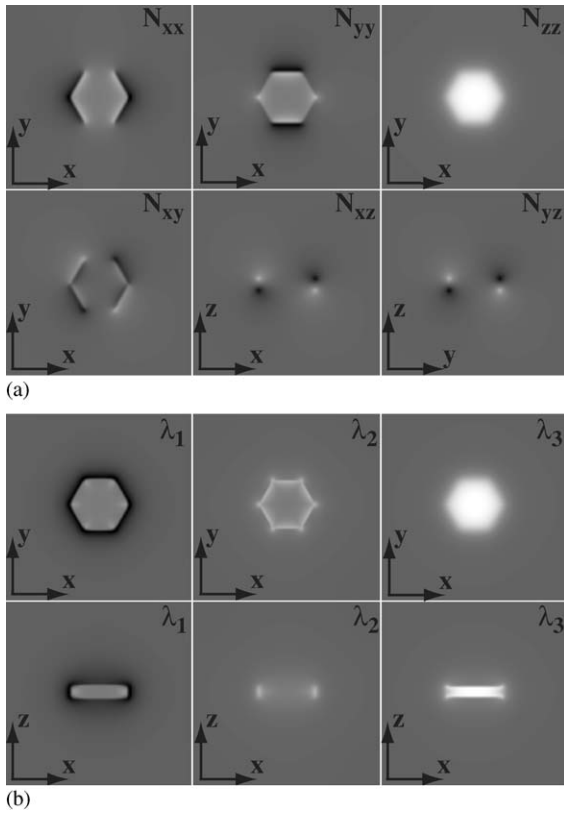


Fig. 5. DTF tensor components (a) and eigenvalues (b) for a hexagonal plate with $c/a = \frac{2}{5}$. The basis vectors indicate the orientation of the planar sections; all sections go through the center of the plate. The eigenvalues are ranked in ascending order. The intensity ranges [black,white] correspond to $[-0.399, 0.784]$ (a) and $[-0.399, 0.789]$ (b).

expression was given in Eq. (26) of Part I. While it is possible to carry out analytically a part of the inverse Fourier transform to compute the DTF $N_{ij}(\mathbf{r})$, we will instead only show numerical results. Care must be taken in the numerical evaluation of the Lommel functions, in particular when the two arguments are large and nearly equal to each other [10,11]. Fig. 6 shows a planar section of the DTF components for three different truncated paraboloids, characterized by $a = h/R^2$. The sections contain the paraboloid center axis. The figure shows the cylindrical components of $N_{ij}(\mathbf{r})$: N_{rr} , $N_{\theta\theta}$, N_{zz} , and N_{rz} .

Fig. 7 shows the eigenvalues of the DTF tensors for the paraboloids shown in Fig. 6. The odd

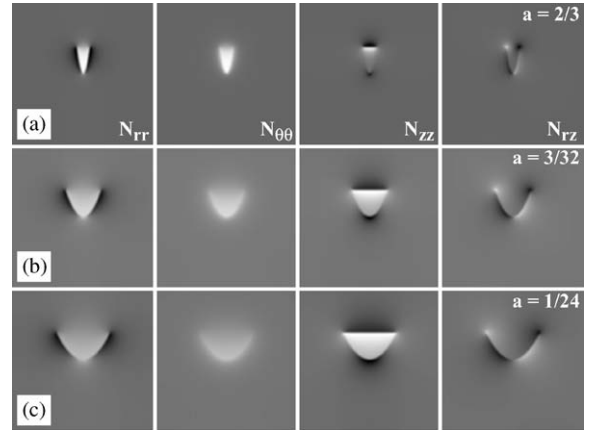


Fig. 6. DTF tensor components, N_{rr} , $N_{\theta\theta}$, N_{zz} and N_{rz} , for three different paraboloids: (a) $a = 2/3$; (b) $a = 3/32$; and (c) $a = 1/24$. The sections contain the paraboloid axis. The intensity range [black,white] corresponds to the ranges $[-0.315, 0.485]$ (a), $[-0.486, 0.566]$ (b) and $[-0.489, 0.635]$ (c).

numbered rows show a section normal to the paraboloid axis at half the height $h/2$, the other rows are sections containing the axis. Eigenvalues are ranked in ascending order. The lowest eigenvalue, λ_1 , varies most strongly outside the particle, while the largest eigenvalue, λ_3 , is mostly important inside the particle. The middle eigenvalue varies both inside and outside the particle. This is a general behavior, observed for many different particle shapes.

4.3. “Pacman”-shaped plates

The opening angle of the “pacman” shape fully determines its geometry. DTF simulations were carried out for the angles $\omega = n\pi/4$ with $n = 1 \dots 4$, and for a particle thickness of $t = R/15$, similar to that used in the experiments reported in Ref. [9]. The results are shown in Fig. 8. For each particle shape, this figure shows the six tensor components as a two-dimensional section through the center of the outer circle of the particle shape (xy section for N_{xx} , N_{xy} , N_{yy} , and N_{zz} , xz section for N_{xz} , and yx section for N_{yz}). The eigenvalues of the DTF are also shown for two different section orientations: xy and xz .

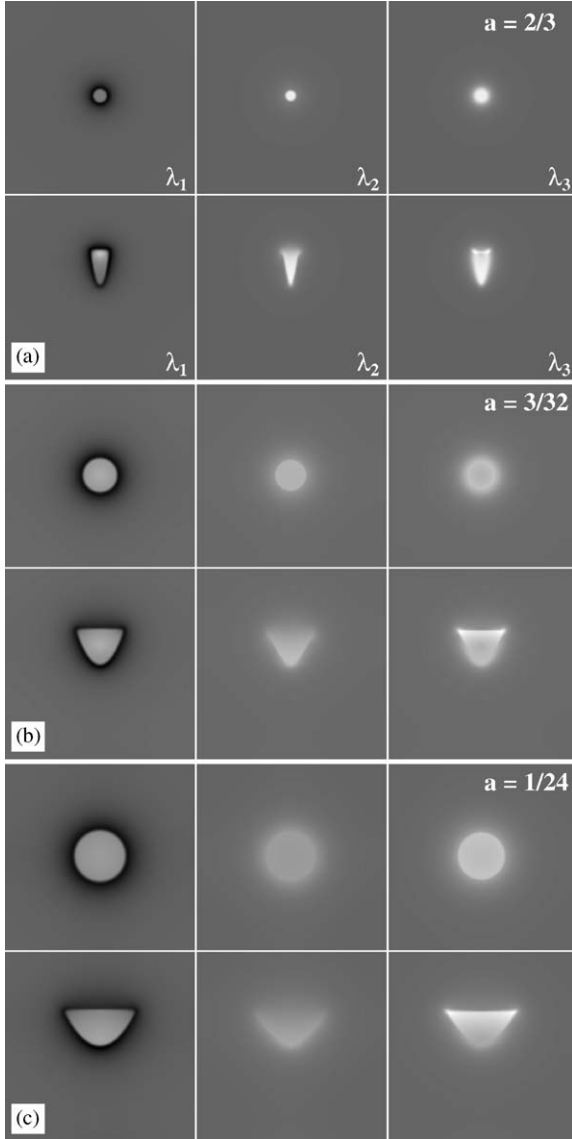


Fig. 7. DTF tensor eigenvalues λ_i ($i = 1 \dots 3$) for the same paraboloids as in Fig. 6. The horizontal sections in the first, third and fifth rows, intersect the paraboloid at half height, the vertical sections in the remaining rows contain the paraboloid axis. The intensity range [black,white] corresponds to the ranges $[-0.318, 0.511]$ (a), $[-0.487, 0.705]$ (b) and $[-0.508, 0.787]$ (c).

The volumetric demagnetization tensor can be computed by means of Eq. (4). Fig. 9 shows the eigenvalues of the volumetric demagnetization factors as a function of the opening angle ω for the pacman shape of Fig. 4(c) (solid lines), as well

as for a simpler shape where the radius r of the inner circle vanishes (dashed lines) (referred to as PM-I in Ref. [9]). The N_{zz} demagnetization factor is about 8% smaller for the new “pacman” shape. This is consistent with the results presented in Ref. [9]; the “pacman” shape of Fig. 9 shows no magnetic domain walls, regardless of the value of the opening angle ω , whereas the shape with $r = 0$ shows a domain with reverse magnetization surrounding the sharp corner at the center of the particle. Rounding of this corner results in a smaller demagnetization field, which favors the single domain state of the particle.

4.4. Computation of the critical aspect ratio for polygonal disks

In Part I, Section 5, we computed analytically the demagnetization energy for the uniformly magnetized cylinder with aspect ratio $\tau = t/2R$, with t the cylinder height and R the radius. It was shown that, if we denote by θ the angle between the magnetization direction and the cylinder axis, the demagnetization energy is proportional to an expression of the following form:

$$E_m(\tau) \sim f_1(\tau)(3 \cos^2 \theta - 1) + f_2(\tau) \cos^2 \theta, \quad (14)$$

where

$$f_1(\tau) = \frac{1}{\tau} \left[\frac{1}{3\pi} - \frac{\sqrt{1-\tau^2}}{4} {}_2F_1 \left[\frac{1}{2}, \frac{3}{2}; 2; \frac{1}{1+\tau^2} \right] \right], \quad (15)$$

$$f_2(\tau) = \frac{1}{2}. \quad (16)$$

The critical aspect ratio τ_c corresponds to a saddle point in the energy (see Fig. 5 in Part I), and can be computed from the condition $3f_1(\tau) + f_2(\tau) = 0$, which leads to $\tau_c = 0.9065$ for the cylinder.

The cylinder can be considered as the limiting case of a series of regular polygonal disks of height t and order N , for $N \rightarrow \infty$. It was shown by Beleggia et al. [6] that the shape amplitude of a regular polygonal disk of order N can be computed analytically. The result is given by

$$D(\mathbf{k}) = 4ic \frac{\text{sinc}(ck_z)}{k_x^2 + k_y^2} \sum_{p=1}^N \sum_{j=1}^3 \kappa_{pj} \text{sinc}(\mu_{pj}) e^{iv_{pj}}, \quad (17)$$

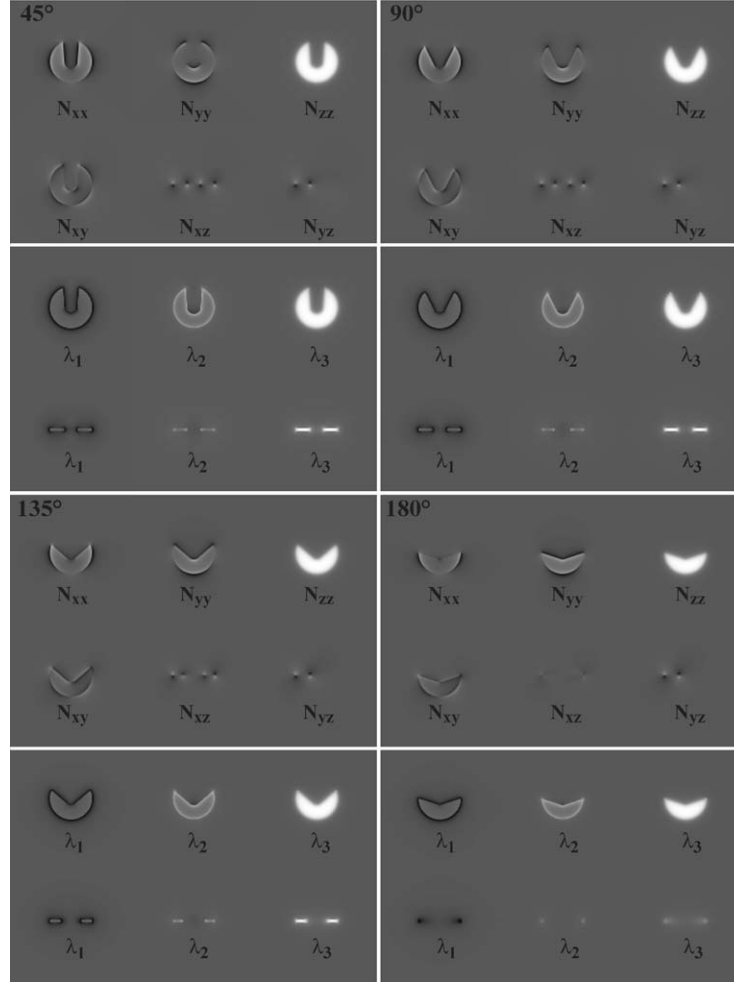


Fig. 8. DTF tensor components and eigenvalues for four different “pacman” shapes. All sections go through the center of the outer circle of the particle shape. The top six figures for each opening angle ω depict sections of the DTF, whereas the bottom two rows depict two sections of the eigenvalues of the DTF in ascending order.

with

$$\kappa_{pj} = [c_p \mu_1 s_p \kappa_1, c_p \mu_2 - s_p \mu_2, -a(s_p k_x + c_p k_y)], \quad (18a)$$

$$\mu_{pj} = [c_p \mu_1 s_p \kappa_1, c_p \mu_2 + s_p \kappa_2, a(c_p k_x - s_p k_y)], \quad (18b)$$

$$v_{pj} = [\mu_{p1}, \mu_{p2}, h(s_p k_x + c_p k_y)], \quad (18c)$$

$c_p = \cos(\theta_p)$, $s_p = \sin(\theta_p)$, $\theta_p = 2p\alpha$, $h = a/\tan\alpha$, and $\alpha = \pi/N$. The parameters κ_i and μ_i are given by

$$\kappa_j = \frac{a}{2}[-\omega k_x + k_y, \omega k_x + k_y], \quad (19a)$$

$$\mu_j = \frac{a}{2}[k_x + \omega k_y, -k_x + \omega k_y], \quad (19b)$$

with $\omega = 1/\tan\alpha$.

Using Eq. (17), we can compute the magnetostatic energy (3) as a function of the angle θ and the aspect ratio $\tau = c/a$ of the polygonal disk, where $c = t/2$, and a is half the edge length. Since each regular polygonal disk has a rotation axis of order N normal to the disk, the magnetostatic energy will be invariant with respect to the azimuthal component of the magnetization direction [3]. This in turn means that the angular

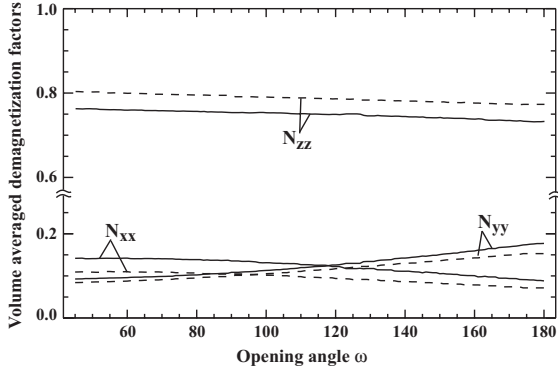


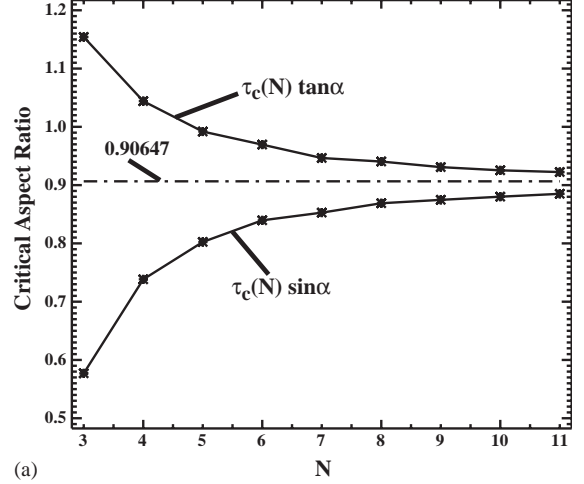
Fig. 9. Comparison between the magnetometric demagnetization factors for the “pacman” shape and a simpler shape for which the radius of the inner circle is equal to zero. The horizontal axis shows the opening angle, as defined in Fig. 4.

integrations will result in the angular dependence of the energy on θ shown for the cylinder in Eq. (14). Therefore, by fitting the energy to the form (14), we obtain both functions $f_i(\tau)$ for a given N . Application of the equation $3f_1(\tau) + f_2(\tau) = 0$ then results in the critical aspect ratio $\tau_c(N)$. Note that the definition of the aspect ratio of the polygonal disk involves the thickness and the edge length, whereas for the cylinder the aspect ratio depends on the thickness and the diameter. We can convert from edge length to either the inscribed or the circumscribed diameter by multiplying the aspect ratio by $\tan \alpha$ or $\sin \alpha$, respectively. The results of numerical simulations for $N = 3 \dots 11$ are shown in Fig. 10. The top curve corresponds to $\tau_c(N)\tan \alpha$, the bottom curve to $\tau_c(N)\sin \alpha$. The dash-dotted line is the analytical value $\tau_c(\infty)$ for the limiting cylinder. It is clear that the two curves for the outer and inner circle converge towards each other and to the critical aspect ratio of the cylinder, when $N \rightarrow \infty$.

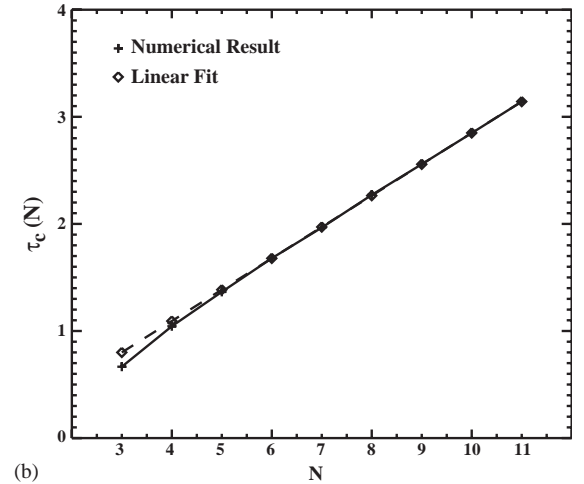
When the critical aspect ratio $\tau_c(N)$ is plotted vs. N , the linear function shown in Fig. 10b is obtained. This linear behavior can be understood as follows: for large N , the critical aspect ratio can be written as

$$\tau_c(N) = c_0 + c_1 N. \quad (20)$$

Converting this aspect ratio to either $\tau_c(N)\tan \alpha$ or $\tau_c(N)\sin \alpha$, and taking the limit for $N \rightarrow \infty$ we must



(a)



(b)

Fig. 10. (a) Critical aspect ratio $\tau_c(N)$ for regular polygonal plates of various orders N , converted to an outer radius value (top curve) and an inner radius value (bottom curve). The dash-dotted line is the limit for $N \rightarrow \infty$, i.e., the cylinder, for which inner and outer radii coincide. (b) Critical aspect ratio as a function of N , along with a linear fit (dashed line). The aspect ratio changes linearly with the order of the polygon for sufficiently large orders.

obtain the critical aspect ratio $\tau_c(\infty)$ for the cylinder:

$$\lim_{N \rightarrow \infty} (c_0 + c_1 N) \begin{cases} \tan \alpha \\ \sin \alpha \end{cases} = \lim_{N \rightarrow \infty} \left(\frac{c_0}{N} + c_1 \right) \pi = c_1 \pi = \tau_c(\infty) = 0.90647, \quad (21)$$

from which follows $c_1 = 0.90647/\pi = 0.28854$. A linear fit to the data of Fig. 10b leads to $c_1 = 0.29276$ and $c_0 = -0.07806$, in reasonable agreement with the theoretical result.

5. Summary

We have presented two accurate and fast numerical methods for the computation of the demagnetization tensor field, the demagnetization energy, and the volumetric demagnetization factors of particles with an arbitrary, finite shape. If an analytical expression for the particle shape amplitude is available, then the DTF can be computed using a 3D inverse FFT operation. To eliminate Gibbs oscillations, which occur due to the intrinsic discontinuous nature of the shape function, $D(\mathbf{r})$, we have proposed a Fourier space filter function. If no explicit expression for the shape amplitude is available, then the DTF can be computed starting from a 3D real space array of 0 and 1 values, defining the shape of the particle. The formalism can also be applied to the computation of magnetostatic self-energy for a particle with an arbitrary shape. It was shown that the critical aspect ratio for the in-plane vs. axial magnetization states in a regular polygonal disk of arbitrary order varies linearly with the order N , for sufficiently large N , and converges to the value for the cylinder. While both the direct space and the Fourier space numerical approaches result in the same accuracy for the demagnetization tensor elements, the Fourier space approach has the advantage of being fast, provided of course that an analytical expression for the shape amplitude can be found. The direct space approach has the advantage that truly arbitrary shapes can be dealt with in a straightforward manner, at the expense of somewhat longer computation times.

While it is difficult in practice to obtain a uniform magnetization in a body of arbitrary shape, accurate knowledge of the DTF for such an object is desirable, in particular in the case of small particles. Below a critical size limit, where the exchange term is largely predominant over other energy contributions, all particles will show a

single domain magnetization state. While there will be small deviations from the uniformly magnetized state, in particular near edges and corners, knowledge of the uniformly magnetized state is useful as a first order approximation to the real magnetization state. The computational methods described in this paper provide a fast and accurate means to access this information. Regarding magnetocrystalline anisotropy, where this effect is not negligible due to the possible polycrystalline nature of the particle, we can simply account for it by specifying the direction of the magnetization along the preferential axis of the particle.

The methods proposed in this paper are based on the use of the fast Fourier transform, for which many speed-optimized implementations are available. Given the simplicity and accuracy of the methods, they should find quick acceptance in the computational magnetism community, and may well replace the slower direct space methods, which often require the numerical evaluation of two 3D integrals.

Acknowledgements

The authors would like to thank Prof. Y.-K. Hong for making available a preprint on the “Pacman”-shaped particles. Financial support was provided by the US Department of Energy, Basic Energy Sciences, under contract numbers DE-FG02-01ER45893 and DE-AC02-98CH10886.

References

- [1] R. Moskowitz, E. Della Torre, IEEE Trans. Magn. 2 (1966) 739.
- [2] S. Tandon, M. Beleggia, Y. Zhu, M. De Graef, J. Magn. Magn. Mater. (2004), *this issue*.
- [3] M. Beleggia, M. De Graef, J. Magn. Magn. Mater. 263 (2003) L1.
- [4] M. Beleggia, Y. Zhu, Philos. Mag. B 83 (2003) 1143.
- [5] J. Komrská, W. Neumann, Phys. Stat. Sol. (a) 150 (1995) 89.
- [6] M. Beleggia, S. Tandon, Y. Zhu, M. De Graef, Philos. Mag. B 83 (2003) 1143.

- [7] M. Frigo, S.G. Johnson, FFTW (Fastest Fourier Transform in the West, version 3.0), URL: <http://www.fftw.org/>, 2003.
- [8] S.K. Park, R.A. Schowengerdt, Comput. Vision, Graphics, Image Process. 23 (1983) 1187.
- [9] M.H. Park, Y.K. Hong, S.H. Gee, D.W. Erickson, B.C. Choi, Appl. Phys. Lett. 83 (2003) 329.
- [10] K.D. Mielenz, J. Res. Natl. Inst. Stand. Technol. 103 (1998) 497.
- [11] W.H. Press, B.P. Flannery, S.A. Teukolsky, W.T. Vetterling, Numerical Recipes: The Art of Scientific Computing (Fortran Version), Cambridge University Press, Cambridge, 1989.